



CHD7 regulates bone-fat balance by suppressing PPAR- γ signaling

Caojie Liu ¹, Qiuchan Xiong¹, Qiwen Li¹, Weimin Lin¹, Shuang Jiang¹, Danting Zhang¹, Yuan Wang¹, Xiaobo Duan¹, Ping Gong ¹✉ & Ning Kang ¹✉

Chromodomain helicase DNA-binding protein 7 (CHD7), an ATP-dependent eukaryotic chromatin remodeling enzyme, is essential for the development of organs. The mutation of *CHD7* is the main cause of CHARGE syndrome, but its function and mechanism in skeletal system remain unclear. Here, we show conditional knockout of *Chd7* in bone marrow mesenchymal stem cells (MSCs) and preosteoblasts leads to a pathological phenotype manifested as low bone mass and severely high marrow adiposity. Mechanistically, we identify enhancement of the peroxisome proliferator-activated receptor (PPAR) signaling in *Chd7*-deficient MSCs. Loss of *Chd7* reduces the restriction of PPAR- γ and then PPAR- γ associates with trimethylated histone H3 at lysine 4 (H3K4me3), which subsequently activates the transcription of downstream adipogenic genes and disrupts the balance between osteogenic and adipogenic differentiation. Our data illustrate the pathological manifestations of *Chd7* mutation in MSCs and reveal an epigenetic mechanism in skeletal health and diseases.

¹State Key Laboratory of Oral Diseases, National Clinical Research Center for Oral Diseases, West China Hospital of Stomatology, Sichuan University, Chengdu 610041, PR China. ✉email: dentistgong@hotmail.com; ningakang20088@163.com

As the common progenitors for osteoblasts and adipocytes, bone marrow mesenchymal stem cells (MSCs) show strict control of cell fate decisions to maintain the balance between osteogenic and adipogenic differentiation to ensure the health of the skeletal system^{1,2}. Characterized by low bone mass and extensive marrow adipose tissue (MAT) accumulation, senile osteoporosis in elderly patients leads to a series of complications, e.g., increasing bone fragility and susceptibility to fracture^{3–5}. Bone marrow MSCs preferentially differentiate into adipocytes under senility or pathological stimuli, e.g., hormone disorders, leading to increased MAT and progressive bone loss^{1,3,6}. Unfortunately, the precise mechanism by which MSC lineage allocation favors adipogenic differentiation toward osteogenic differentiation remains to be explored.

As typical ATP-dependent eukaryotic chromatin remodeling enzymes, the members of the chromodomain helicase DNA-binding protein (CHD) superfamily interrupt the interaction between DNA and chromatin by translocating nucleosomes along the DNA strand^{7,8}. The CHD family is essential for the expression of normal genes and the maintenance of dynamic chromatin structure via their ability to activate or suppress specific histone markers^{9,10}. Hence, the CHD superfamily is critical for the maintenance and proliferation of stem cells, in addition to cell differentiation and cell fate decisions^{11,12}.

As one of the most researched members of the CHD family, CHD7 is widely expressed in various tissues and plays a critical role in the development of organs^{10,12}. Mutation of *CHD7* is the main cause of CHARGE syndrome, a kind of developmental disorder involving multiple organ system defects, characterized as coloboma of the eye, heart defects, atresia of the choanae, retarded growth, genital anomalies, ear malformations and deafness^{13–15}. The acronym of these six major manifestations was defined as CHARGE syndrome in 1981¹⁶.

As previously indicated, CHD7 is an ATP-dependent chromatin remodeling enzyme that regulates the location of nucleosomes and alters DNA accessibility^{17,18}. According to previous studies, one of the main functions of the CHD family is binding to methylated histone residues and promoting methylated histone H3 at lysine 4 (H3K4me) interactions^{8,19}. Previously found by chromatin immunoprecipitation (ChIP), CHD7 recruitment was strongly linked to histone modification, e.g., colocalization with H3K4me1 at the enhancer subregion and with H3K4me3 at the promoters of the transcription initiation site²⁰.

We previously showed that CHD7 could promote the osteogenic differentiation of human bone MSCs by interacting with SMAD1 and binding to the enhancer region of *SP7*²¹. In this work, we generated *Chd7* conditional knockout mice and unveiled the essential role of CHD7 in MSC fate decisions by suppressing the peroxisome proliferator-activated receptor gamma (PPAR- γ) signaling pathway. Such findings might provide insight into the pivotal regulatory role of CHD7 in bone development and diseases, as well as a probable clinical therapeutic strategy.

Results

Deletion of *Chd7* in MSCs leads to skeletal development disorder. To investigate the potential role of CHD7 in skeletal development, we examined the expression of CHD7 in mouse femurs. Immunohistochemical (IHC) staining showed that CHD7 was prevalently expressed in the nuclei of bone cells and bone marrow in both primary and secondary ossification centers but marginally expressed in chondrocytes of the growth plate (Supplementary Fig. 1a). Immunofluorescence (IF) staining images showed the same trend (Supplementary Fig. 1b).

Next, we generated *Chd7* flox (*Chd7*^{flox/+}) mice via the CRISPR/Cas9 technique and then mated them with *Prx1-cre* transgenic mice

to generate conditional homozygous *Chd7* knockout mice, *Prx1-cre;Chd7*^{flox/flox} (Supplementary Fig. 1c, d). The birth status and the gender ratio of the pups were basically consistent with Mendelian law. *Prx1-cre;Chd7*^{flox/flox} mice were viable, although with a relatively lower survival rate (Supplementary Fig. 1e). The *Prx1-cre;Chd7*^{flox/flox} mice had a smaller size, a lighter weight, and delayed growth features compared to their *Chd7*^{flox/flox} control littermates at 4 weeks after birth (Fig. 1a, Supplementary Fig. 1f). The IHC and IF staining images of the *Prx1-cre;Chd7*^{flox/flox} mice confirmed the successful deletion of *Chd7* in MSCs (Supplementary Fig. 1a, b).

We conducted whole-mount skeletal staining on pups 2 days after birth and observed that the skeletal development of *Prx1-cre;Chd7*^{flox/flox} pups is significantly delayed compared with that of *Chd7*^{flox/flox} littermates, with shorter forelimbs and hindlimbs and a lower degree of mineralization in the cranial and maxillofacial bone (Fig. 1b, c). The skulls of 2-week-old and 4-week-old mice were harvested and scanned by microcomputed tomography (microCT). The reconstructed images showed nonclosure of fontanels in the *Prx1-cre;Chd7*^{flox/flox} mice, indicating that knockout of *Chd7* in MSCs leads to cranial bone hypoplasia (Fig. 1d, e).

Deletion of *Chd7* in MSCs leads to low bone mass and high marrow adiposity. MicroCT analysis of distal femur metaphysis indicated that bone mineral density (BMD) and bone volume/tissue volume ratio (BV/TV) were significantly reduced in both male and female *Prx1-cre;Chd7*^{flox/flox} mice compared to their *Chd7*^{flox/flox} littermates at 4 weeks of age. In addition, *Chd7* deletion impaired the trabecular number (Tb.N), the trabecular thickness (Tb.Th) and the midshaft cortical thickness (Ct.Th), while elevating the trabecular separation (Tb.Sp) (Fig. 2a, b).

The undecalcified sections after Von Kossa staining further validated the low bone mass phenotype of the *Prx1-cre;Chd7*^{flox/flox} mice (Fig. 2c). The *Prx1-cre;Chd7*^{flox/flox} mice also showed a slower mineral apposition rate (MAR) and bone formation rate (BFR) (Fig. 2e). In addition, the *Prx1-cre;Chd7*^{flox/flox} mice had fewer osteoblasts (N.Ob/B.Pm), indicating a diminished bone formation. The osteoclast number (N.Oc/B.Pm) showed no obvious differences between groups (Fig. 2d, e). *Chd7* knockout also led to a slightly shortened growth plate (Supplementary Fig. 1a).

Notably, in both male and female *Prx1-cre;Chd7*^{flox/flox} mice, the loss of bone mass was associated with obviously increased bone marrow adipose tissue accumulation in both the primary and secondary ossification centers (Fig. 2f). The number and density of bone marrow adipocytes were apparently elevated in the *Prx1-cre;Chd7*^{flox/flox} mice (Fig. 2g). For unknown reasons, the phenotype of increased MAT was more striking in female *Prx1-cre;Chd7*^{flox/flox} mice.

Loss of *Chd7* in preosteoblasts leads to low bone mass and high marrow adiposity. To further investigate whether depletion of *Chd7* from committed osteoblast progenitors could induce a similar bone loss phenotype, we mated the *Sp7-cre* transgenic mice with the *Chd7*^{flox/flox} mice²⁸. The *Sp7-cre;Chd7*^{flox/flox} mice also exhibited a smaller size, lighter weight, lower survival rate and delayed growth features (Supplementary Fig. 2a, b). MicroCT analysis of the femur metaphysis revealed a diminishment in trabecular and cortical bone in the *Sp7-cre;Chd7*^{flox/flox} mice, as shown by impaired skeletal parameters, e.g., BMD, BV/TV, Tb.N, Tb.Th and Ct.Th, and elevated Tb.Sp (Fig. 3a, b).

The Von Kossa staining validated the low bone mass phenotype of the *Sp7-cre;Chd7*^{flox/flox} mice (Fig. 3c). The *Sp7-cre;Chd7*^{flox/flox} mice also showed declined dynamic skeletal histomorphometric features, manifested as slower MAR and BFR (Fig. 3e). In addition, the decrease in osteoblast numbers further confirmed the osteopenic manifestations of the *Sp7-cre;Chd7*^{flox/flox} mice (Fig. 3d, e).

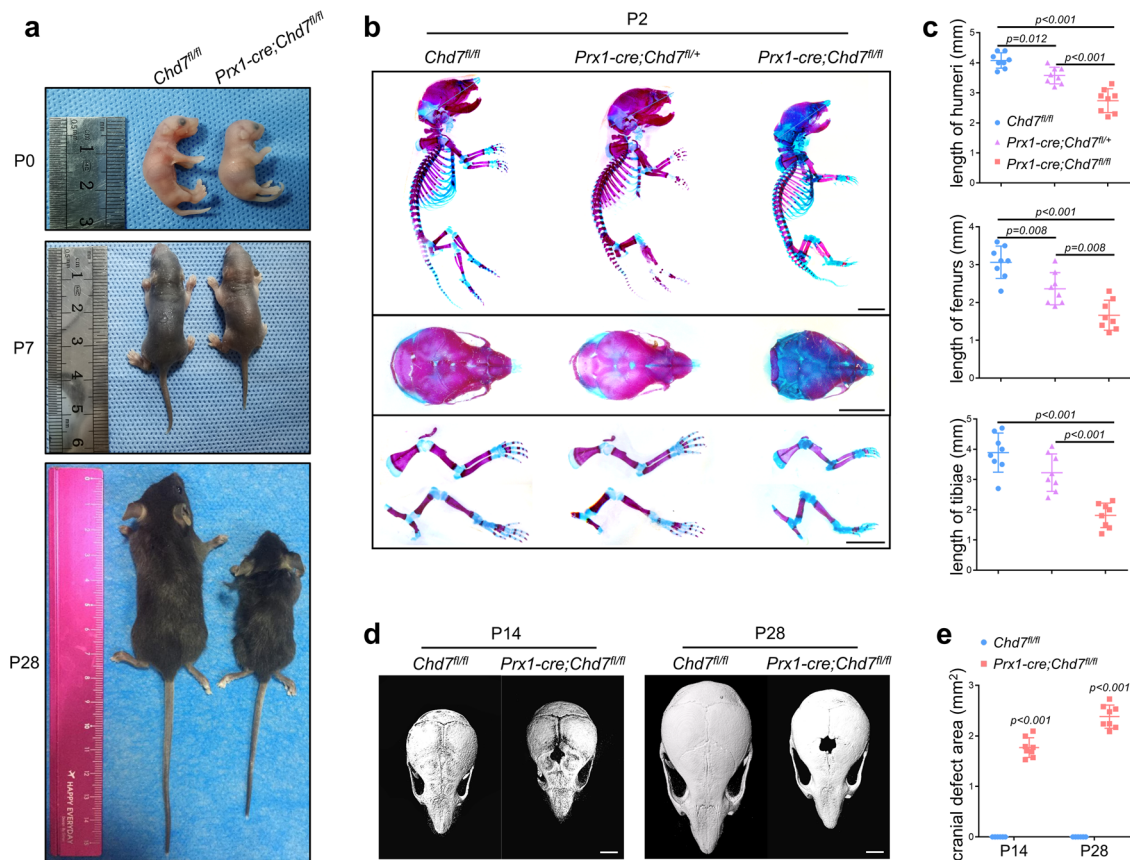


Fig. 1 Deletion of *Chd7* in MSCs leads to skeletal development disorder. **a** Representative images of the *Chd7^{fl/fl}* and *Prx1-cre;Chd7^{fl/fl}* mice at postnatal day 0, day 7, and day 28. **b** Alizarin red/Alcian blue whole-mount skeletal staining images of the *Chd7^{fl/fl}*, *Prx1-cre;Chd7^{fl/+}*, and *Prx1-cre;Chd7^{fl/fl}* pups at postnatal day 2. Compared to the control littermates, the *Prx1-cre;Chd7^{fl/fl}* pups had shorter forelimbs and hindlimbs and a lower degree of mineralization in the cranial and maxillofacial bone. Scale bar, 5 mm. **c** Quantification of (b), including the length of humeri, femurs, and tibiae of the mice at postnatal day 2 ($n = 8$). **d** Representative reconstructed microCT images of skulls of the 2-week-old and 4-week-old *Chd7^{fl/fl}* and *Prx1-cre;Chd7^{fl/fl}* mice. The skulls of *Prx1-cre;Chd7^{fl/fl}* mice showed nonclosure of fontanel. Scale bar, 2 mm. **e** Quantification of (d), cranial defect area calculated by ImageJ ($n = 8$). Data are shown as the mean \pm S.D.; p value by two-tailed for independent sample tests or one-way ANOVA with Tukey's post hoc tests for multiple comparisons.

Similarly, increased MAT accumulation was also observed in both the primary and secondary ossification centers of femurs from the *Sp7-cre;Chd7^{fl/fl}* mice (Fig. 3f, g). Moreover, the MAT accumulation phenomena were more remarkable in the tibia of the *Sp7-cre;Chd7^{fl/fl}* mice at the age of 4 weeks. Considerable MAT was observed at the mesial region, while the distal region was mostly occupied by MAT, with a very small amount of bone tissue left at the distal region of tibiae in the female *Sp7-cre;Chd7^{fl/fl}* mice (Supplementary Fig. 2c).

***Chd7*-deficient MSCs exhibit reduced osteogenic and increased adipogenic potential.** Next, we sought to isolate MSCs from the *Chd7^{fl/fl}* and *Prx1-cre;Chd7^{fl/fl}* mice and compared their osteogenic and adipogenic potential in vitro (Supplementary Fig. 3a). Flow cytometry was conducted to identify the primary mouse bone marrow mesenchymal stem cells with anti-CD29 and anti-CD90.2 antibodies.

After osteogenic induction, lighter alkaline phosphatase (ALP) staining indicated the incompetent osteogenic differentiation of the *Chd7*-deleted MSCs (Fig. 4a). Meanwhile, impaired ALP activity and less calcium mineralization were detected in the *Prx1-cre;Chd7^{fl/fl}* MSCs (Fig. 4a–c). The significantly down-regulated expression of osteogenic markers, e.g., *Dlx5*, *Runx2*, *Sp7*, *Bmp2*, and *Bglap*, strengthened the reduced osteogenic potential of *Chd7*-deficient MSCs (Fig. 4d, e).

After adipogenic induction, the elevated intensity of Nile red staining demonstrated obviously increased lipid droplet in the *Chd7*-deleted MSCs (Fig. 4f). Meanwhile, significantly upregulated expression of classic adipogenic genes, e.g., *Cebpa*, *Pparg*, *Adipoq*, *Plin1*, and *Cd36*, indicated the intensified adipogenic potential of the *Prx1-cre;Chd7^{fl/fl}* MSCs (Fig. 4g).

CHD7 suppresses the transactivation of PPAR- γ . Next, we performed RNA-seq of MSCs to identify the critical mechanism. Gene set enrichment analysis (GSEA) confirmed the restricted osteogenesis in *Prx1-cre;Chd7^{fl/fl}* MSCs after osteogenic induction (Fig. 5a, b). Interestingly, significant enhancement of the PPAR signaling pathway was found in the *Prx1-cre;Chd7^{fl/fl}* group, indicating that the PPAR family might play a crucial role in the formation of the abovementioned phenotype (Fig. 5a).

Meanwhile, among MSCs after adipogenic induction, significant enhancement of the PPAR signaling pathway was also found in the *Prx1-cre;Chd7^{fl/fl}* group, along with enhancement of the adipogenesis pathway and increased expression of downstream genes of PPAR- γ (Fig. 5c, d).

Next, we sought to verify whether CHD7 directly interacts with PPAR- γ by conducting a coimmunoprecipitation (co-IP) assay. In MSCs isolated from *Chd7^{fl/fl}* mice, CHD7 was successfully detected in PPAR- γ immunoprecipitates (Fig. 5e). However, H3K4me3 was barely observed in PPAR- γ immunoprecipitates,

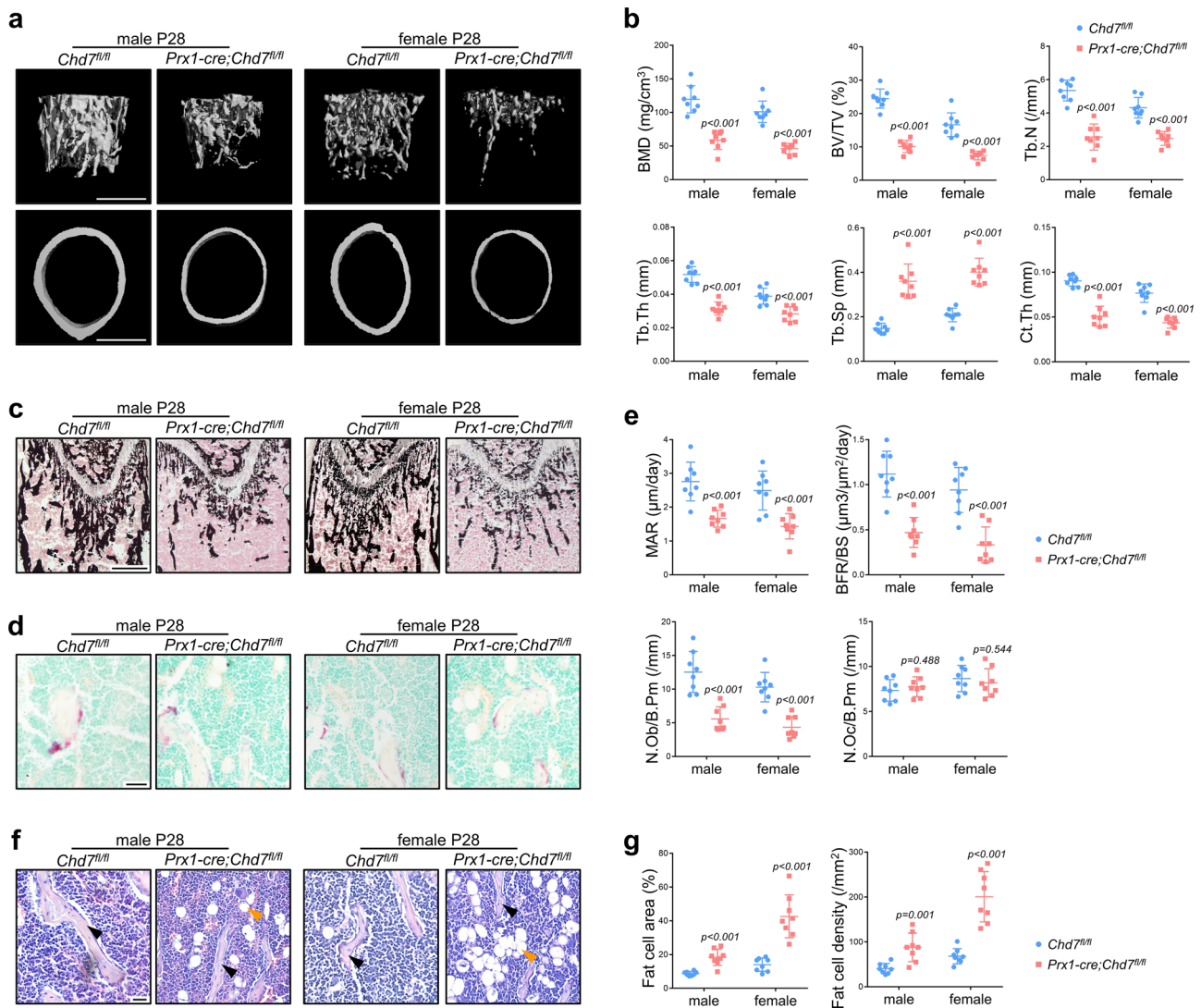


Fig. 2 Deletion of *Chd7* in MSCs leads to low bone mass and high marrow adiposity. **a** Representative microCT images of distal femurs and midshaft cortical bone from *Chd7^{fl/fl}* and *Prx1-cre;Chd7^{fl/fl}* mice at 4 weeks old (Scale bar, 500 μ m). **b** Quantitative microCT analyses of the distal end of the femurs from *Chd7^{fl/fl}* and *Prx1-cre;Chd7^{fl/fl}* mice at 4 weeks old ($n = 8$). **c** Von Kossa staining of undecalcified sections of femurs from *Chd7^{fl/fl}* and *Prx1-cre;Chd7^{fl/fl}* mice at 4 weeks old (Scale bar, 500 μ m). **d** TRAP staining of femur sections from *Chd7^{fl/fl}* and *Prx1-cre;Chd7^{fl/fl}* mice at 4 weeks old (Scale bar, 50 μ m). **e** Dynamic osteogenic index of trabecular bone from the femoral metaphysis in *Chd7^{fl/fl}* and *Prx1-cre;Chd7^{fl/fl}* mice at 4 weeks old, including MAR and BFR determined by double labeling ($n = 8$). Histomorphological analysis of trabecular bone from the femoral metaphysis in *Chd7^{fl/fl}* and *Prx1-cre;Chd7^{fl/fl}* mice at 4 weeks old, including osteoblast and osteoclast numbers ($n = 8$). **f** Representative images of adipocytes in the distal femur marrow in *Chd7^{fl/fl}* and *Prx1-cre;Chd7^{fl/fl}* mice at 4 weeks old. Black arrows indicate trabecular bones, and orange arrows indicate marrow adipose tissues (Scale bar, 50 μ m). **g** Quantitative measurements of adipocytes, including number and area of adipocytes in the distal marrow per tissue area. Quantitative data were obtained using the ImageJ software ($n = 8$). Data are shown as the mean \pm S.D.; p value by two-tailed Student's t test.

indicating that PPAR- γ might not be activated in wild-type MSCs. In contrast, H3K4me3 was detected in PPAR- γ immunoprecipitates in the *Chd7*-deficient MSCs (Fig. 5e). To intuitively observe the altered binding pattern of PPAR- γ and H3K4me3, we conducted IF staining to detect their colocalization within the nucleus. In the *Prx1-cre;Chd7^{fl/fl}* MSCs, the merged rates of PPAR- γ and H3K4me3 were significantly higher than those in wild-type MSCs, in accordance with the co-IP assay (Fig. 5f, g).

Next, we aimed to determine how this binding alteration regulates cell fate decisions. By analyzing ChIP-sequencing (ChIP-seq) data of *Mus musculus* (GSM2104246 and GSM1571714)^{29,30}, we confirmed that H3K4me3 and PPAR- γ could coaggregate at the promoter region of *Adipoq* (Fig. 5h). On this basis, we performed a ChIP-PCR assay on the MSCs. The enrichment of H3K4me3 and PPAR- γ at the promoter regions of

Adipoq was significantly increased in MSCs isolated from *Prx1-cre;Chd7^{fl/fl}* mice (Fig. 5i, j).

PPAR- γ inhibition partially rescues the phenotype of *Chd7*-deficient MSCs. To verify that activated PPAR- γ contributed to pathogenic phenotype upon *Chd7* depletion, we treated the *Prx1-cre;Chd7^{fl/fl}* MSCs with the PPAR- γ -specific antagonist GW9662. Although the protein level of CHD7 in the *Prx1-cre;Chd7^{fl/fl}* MSCs was unchanged, the expression of PPAR- γ was significantly restricted. Meanwhile, the PPAR- γ antagonist partially recovered the expression of RUNX2 and alkaline phosphatase (Fig. 6a).

After osteogenic induction, the increases in ALP, ARS staining, and ALP activity indicated the partially restored osteogenic differentiation of the treated *Chd7*-deleted MSCs (Fig. 6b–d).

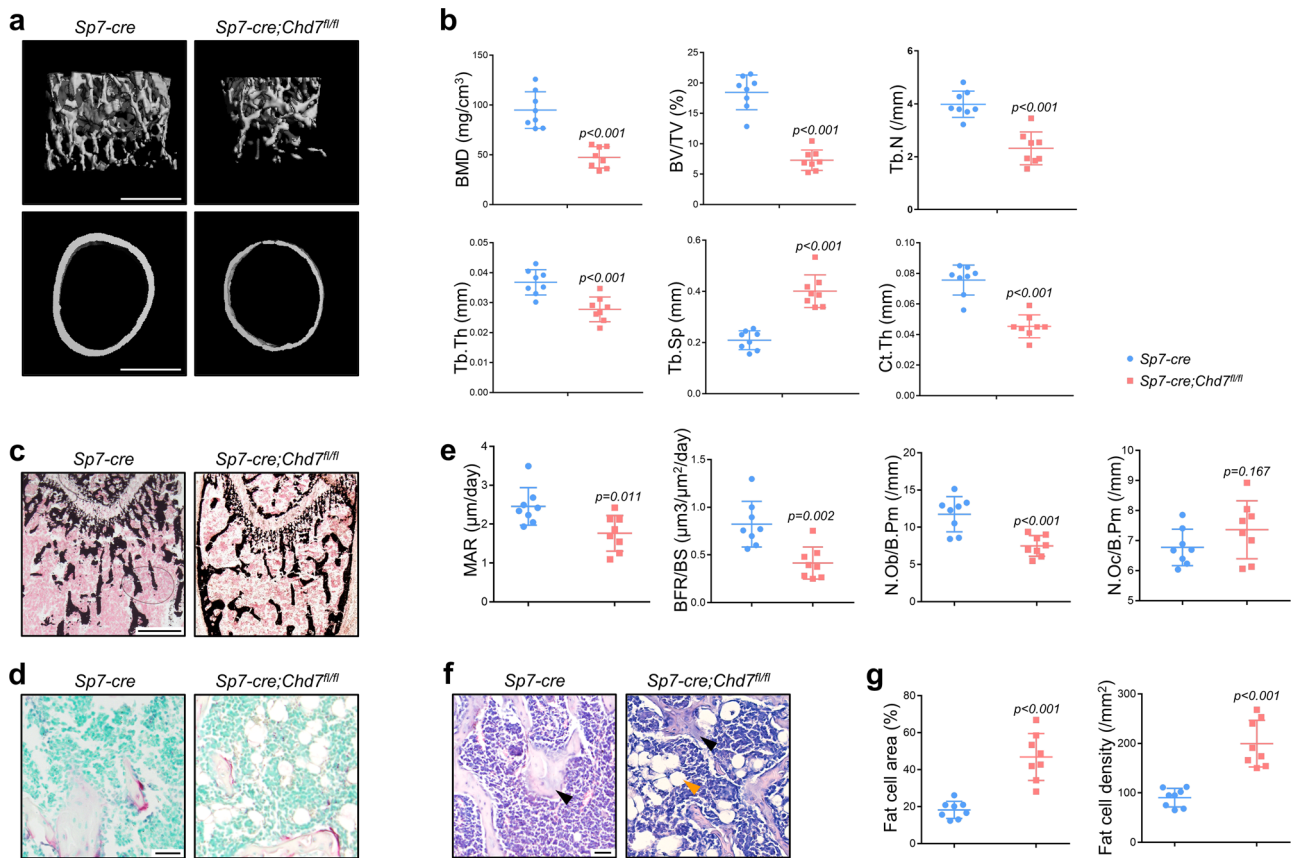


Fig. 3 Loss of *Chd7* in preosteoblasts leads to low bone mass and high marrow adiposity. **a** Representative microCT images of distal femurs and midshaft cortical bone from *Sp7-cre* and *Sp7-cre;Chd7^{fl/fl}* mice at 4 weeks old (Scale bar, 500 μ m). **b** Quantitative microCT analyses of the distal end of the femur from *Sp7-cre* and *Sp7-cre;Chd7^{fl/fl}* mice at 4 weeks old ($n = 8$). **c** Von Kossa staining of undecalcified sections of femurs from *Sp7-cre* and *Sp7-cre;Chd7^{fl/fl}* mice at 4 weeks old (Scale bar, 500 μ m). **d** TRAP staining of femur sections from *Sp7-cre* and *Sp7-cre;Chd7^{fl/fl}* mice at 4 weeks old (Scale bar, 50 μ m). **e** Dynamic osteogenic index of trabecular bone from the femoral metaphysis in *Sp7-cre* and *Prx1-cre;Chd7^{fl/fl}* mice at 4 weeks old, including MAR and BFR determined by double labeling ($n = 8$). **f** Histomorphological analysis of trabecular bone from the femoral metaphysis in *Sp7-cre* and *Prx1-cre;Chd7^{fl/fl}* mice at 4 weeks old, including osteoblast and osteoclast numbers ($n = 8$). **g** Representative images of adipocytes in the distal femur marrow in *Sp7-cre* and *Prx1-cre;Chd7^{fl/fl}* mice at 4 weeks old. Black arrows indicate trabecular bones, and orange arrows indicate marrow adipose tissues (Scale bar, 50 μ m). **g** Quantitative measurements of adipocytes, including number and area of adipocytes in the distal marrow per tissue area. Quantitative data were obtained using the ImageJ software ($n = 8$). Data are shown as the mean \pm S.D.; p value by two-tailed Student's t test.

Meanwhile, the upregulated expression of osteogenic markers, e.g., *Dlx5*, *Runx2*, *Sp7*, strengthened the recovered osteogenic potential of treated *Chd7*-deficient MSCs (Fig. 6e).

After adipogenic induction, the weakened intensity of Nile red staining demonstrated decreased lipid droplet in the treated *Chd7*-deleted MSCs (Fig. 4f). Meanwhile, downregulated expression of classic adipogenic genes, e.g., *Cebpa*, *Pparg*, *Adipoq*, indicated the restricted adipogenic potential of the treated *Prx1-cre;Chd7^{fl/fl}* MSCs (Fig. 4g).

Administration of a PPAR- γ inhibitor partially rescues the skeletal phenotype of *Prx1-cre;Chd7^{fl/fl}* mice. Intraperitoneal injection of the PPAR- γ inhibitor GW9662 partially recovered the body size and weight of the *Prx1-cre;Chd7^{fl/fl}* mice (Fig. 7a–c). MicroCT analysis of the femur metaphysis showed partially recovered trabecular and cortical bone in the treated *Prx1-cre;Chd7^{fl/fl}* mice, as shown by recovered skeletal parameters, e.g., BMD, BV/TV, Tb.N, Tb.Th, Ct.Th, and Tb.Sp (Fig. 7d, e).

The Von Kossa staining validated the restored bone mass of the treated *Prx1-cre;Chd7^{fl/fl}* mice (Fig. 7f). The treated *Prx1-cre;Chd7^{fl/fl}* mice also showed recovered skeletal histomorphometric features, manifested as elevated BFR and increased osteoblast numbers (Fig. 7g).

Moreover, decreased MAT accumulation was also observed in femurs from the treated *Prx1-cre;Chd7^{fl/fl}* mice (Fig. 7h). The number and density of bone marrow adipocytes were evidently reduced in the treated *Prx1-cre;Chd7^{fl/fl}* mice (Fig. 7i). Consequently, the three major manifestations of *Chd7* depletion in MSCs—whole-body skeletal system development disorder, low bone mass, and high marrow adiposity—could be partially rescued by administration of a PPAR- γ inhibitor.

Discussion

As a dynamic process, stem cell differentiation is regulated by activating or suppressing a specific locus and dividing the genome into transcriptionally active or inactive chromodomains^{31,32}. Epigenetic regulation plays an essential role in the growth and development of multiple organ systems in mammals, e.g., DNA methylation, histone modification, chromosome remodeling, and RNA interference^{33,34}. As a hotspot in current research, the methylation and acetylation of histone lysines is a crucial modification at the tails of histones, playing an important role in stem cell differentiation and even cell fate decisions^{35,36}. Generally, H3K4me1 is considered as a marker of enhancers, while H3K4me2 and H3K4me3 modifications are mostly enriched at promoters near transcription initiation sites to activate specific

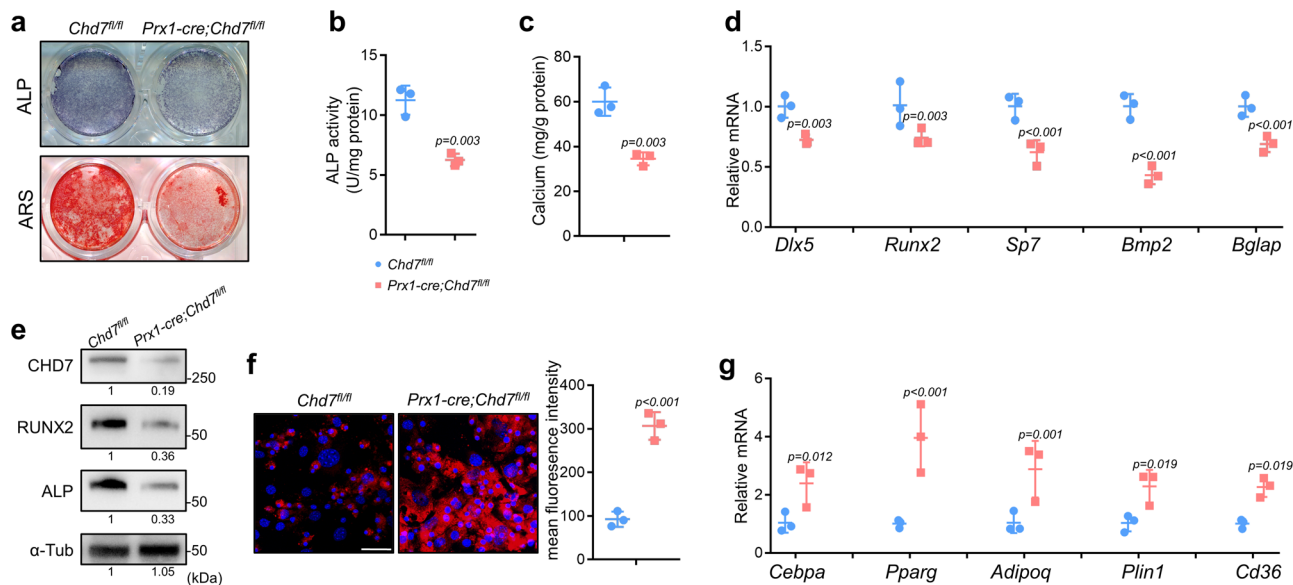


Fig. 4 *Chd7*-deficient MSCs exhibit reduced osteogenic and increased adipogenic potential. **a** Representative images of ALP and ARS staining in MSCs. **b** Quantitative analyses of the ALP activity ($n = 3$ biologically independent MSC sample). **c** Quantitative analyses of the mineralization ($n = 3$ biologically independent MSC sample). **d** qRT-PCR analyses of the mRNA expression of *Dlx5*, *Runx2*, *Sp7*, *Bmp2*, and *Bglap* in MSCs under osteogenic conditions ($n = 3$ biologically independent MSC sample). **e** Western blot analysis and quantification of CHD7, RUNX2 and alkaline phosphatase in bone marrow MSCs isolated from the *Chd7^{fl/fl}* and *Prx1-cre;Chd7^{fl/fl}* mice. **f** Representative images and quantitative analyses of Nile red staining in MSCs. Scale bar, 50 μm ($n = 3$ biologically independent MSC slides). **g** qRT-PCR analyses of the mRNA expression of *Cebpa*, *Pparg*, *Adipoq*, *Plin1*, *CD36* in MSCs under adipogenic conditions ($n = 3$ biologically independent MSC samples). Data are shown as the mean \pm S.D.; p value by two-tailed Student's t test.

gene expression^{20,37–39}. Acetylated histone H3 at lysine 27 (H3K27ac) is defined as a superenhancer that upregulates gene expression, while H3K9me3 and H3K27me3 are universally recognized as suppressive transcriptional modifications^{36,40–44}.

Accumulating evidence has uncovered the regulatory role of CHD7 in epigenetics. As reported previously, in mammals, CHD7 could be recruited at the promoters or superenhancers of the transcriptionally active region of specific genes to increase or decrease transcription^{20,45}. Existing studies of CHD7 preferentially shed light on nervous system development and the differentiation of neural stem cells and neural crest stem cells, and CHD7 has been proven to be crucial for neurogenesis and adult neural stem cell maintenance^{9,10,13,46,47}. Widely observed in clinical work, the alteration of CHD7 expression levels in specific cell lineages leads to severe malfunction or diseases, e.g., CHARGE syndrome, Kallmann syndrome, autism spectrum disorder, developmental disorders of multiple organ systems, and tumorigenesis^{13,15,45–49}. Some of these conditions were caused by the mutation of *CHD7*, while others resulted from changes in CHD7 histone modification or chromatin remodeling functions^{45,48–50}.

Here, we discovered that CHD7 regulates osteogenesis and cell fate decisions in bone marrow MSCs by suppressing the PPAR- γ signaling pathway. By using different temporal markers of osteogenic stem cells, *Prx1* and *Sp7*, we established two lines of transgenic mice to conditionally knockout *Chd7* from the limb bud mesenchyme at a very early time or from preosteoblasts at the initial stage of differentiation^{27,28}. We found that loss of *Chd7* in MSCs disrupted the cell fate decision in mice, leading to the pathological manifestations of osteoporosis, e.g., low bone mass with an impaired osteogenic capacity, as well as high marrow adiposity with an enhanced adipogenic ability, revealing the effective and specific regulation of CHD7 on MSCs.

Previously, PPAR- γ was reported to act as a pivotal nuclear receptor and regulate stem cell differentiation and cell fate decisions⁵¹. This process relies on the association with coactivators or corepressors cooperating with the methylation and

acetylation of histone lysine⁵². Admittedly, osteogenesis, adipogenesis, and chondrogenesis are three major directions of the multidirectional differentiation potential of MSCs. The activation of PPAR- γ primarily drives the cell fate of MSCs to adipogenesis^{52,53}. However, via the inhibiting function of PPAR- γ of specific progenitor cytokines or other corepressors, the cell fate of MSCs favoring adipogenic differentiation could also be reversed toward osteogenic differentiation^{53,54}. Consistent with our findings, the enhanced PPAR signaling pathway was consistent with the phenotype of the *Prx1-cre;Chd7^{fl/fl}* mice in vivo and in vitro. Further, the administration of a PPAR- γ antagonist largely converted the biased MSC adipogenic differentiation and allowed osteogenesis to dominate, which also further confirmed the PPAR signaling pathway as an innovative mechanism whereby CHD7-mediated histone modification manipulated the cell lineage allocation of bone marrow MSCs.

Our findings indicated that when CHD7 bound PPAR- γ , the interaction between PPAR- γ and H3K4me3 was reduced, and consequently, the expression of the downstream adipogenic genes were downregulated, while that of osteogenic-related genes was upregulated, leading to the osteogenic differentiation of MSCs. In contrast, when CHD7 was depleted in MSCs, PPAR- γ colocalized with and contacted H3K4me3 and then activated the transcription of downstream adipogenic genes, leading to the adipogenic differentiation of MSCs (Supplementary Fig. 4a).

Notably, no significant difference ($p > 0.05$) in the osteoclast number (N.Oc/B.Pm) was found between the *Prx1-cre;Chd7^{fl/fl}* mice and their *Chd7^{fl/fl}* control littermates. We speculated that such minor alterations might not be the major factor of the low bone mass in the *Prx1-cre;Chd7^{fl/fl}* mice. According to a previous study, bone marrow adipocytes might be the source of RANKL²³. Therefore, the minor alteration of the osteoclast number in the *Prx1-cre;Chd7^{fl/fl}* mice might be a side effect of MAT accumulation, which deserves further research.

Certain limitations in our work should be listed to provide ideas for further research. The MAT accumulation in bone

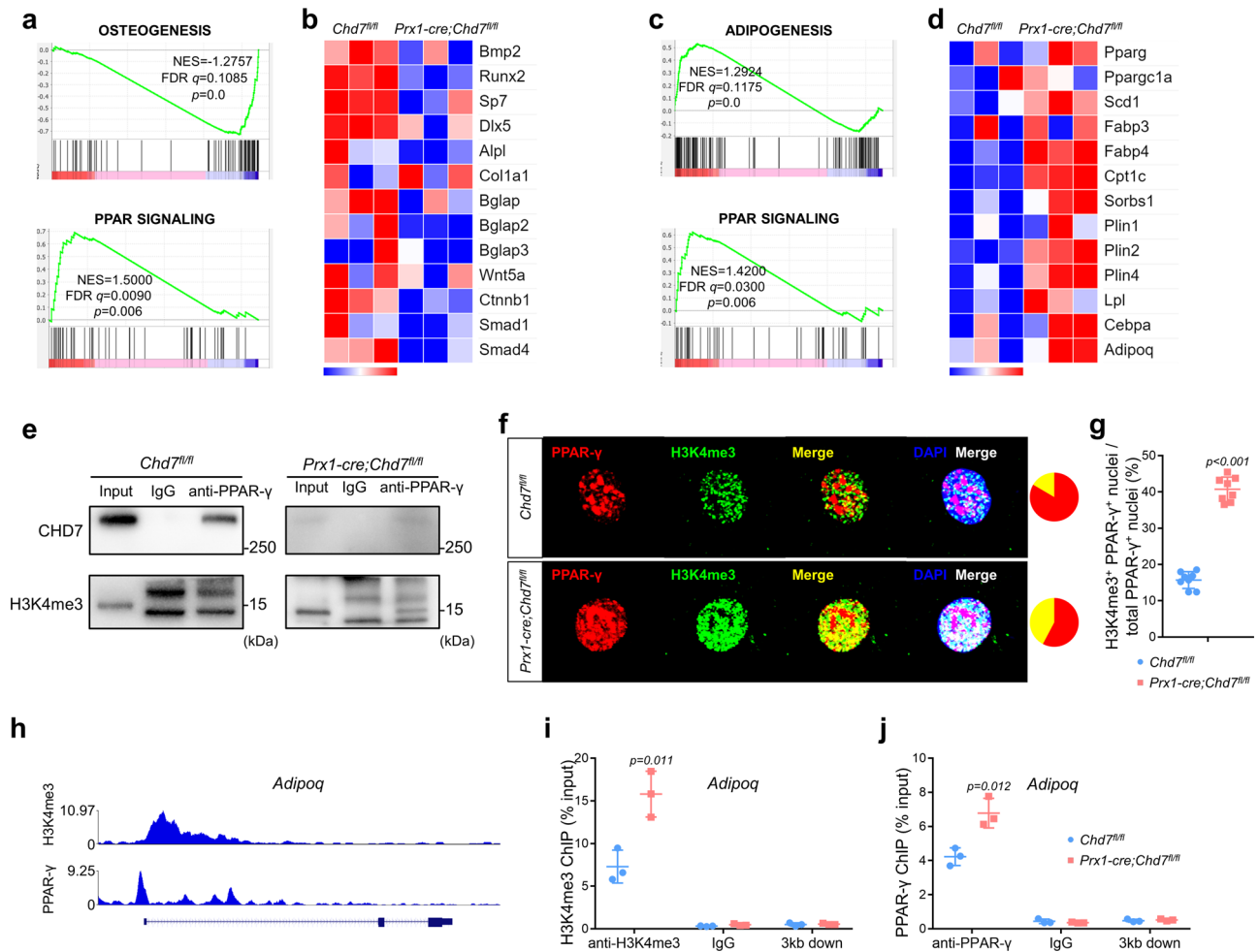


Fig. 5 CHD7 suppresses the transactivation of PPAR-γ. **a** GSEA showing decreased enrichment of osteogenesis-related genes and increased enrichment of PPAR-regulated genes in the *Chd7*-deficient MSCs under osteogenic conditions. **b** Heatmap of representative osteogenesis-associated genes in the *Chd7*-deficient MSCs under osteogenic conditions. **c** GSEA showing increased enrichment of adipogenesis-related genes and PPAR-regulated genes in the *Chd7*-deficient MSCs under adipogenic conditions. **d** Heatmap of representative PPAR signaling pathway-associated genes in the *Chd7*-deficient MSCs under adipogenic conditions. **e** Immunoprecipitation assay in MSCs from the *Chd7^{fl/fl}* and *Prx1-cre;Chd7^{fl/fl}* mice. Cell extracts were immunoprecipitated with anti-PPAR-γ antibodies. Immunoprecipitates were detected by western blotting with the indicated antibodies. **f** Representative immunofluorescence staining of PPAR-γ and H3K4me3 in MSCs from the *Chd7^{fl/fl}* and *Prx1-cre;Chd7^{fl/fl}* mice (Scale bar, 20 μm). **g** Quantification of (f), showing the proportion of H3K4me3⁺ PPAR-γ⁺ nuclei among the total PPAR-γ⁺ nuclei (n = 8). **h** ChIP-seq results indicating that H3K4me3 and PPAR-γ coaggregate near the promoter region of *Adipoq* by WashU EpiGenome Browser. **i** ChIP-qPCR showing that knockout of *Chd7* increases the occupancy of H3K4me3 in the promoter regions of *Adipoq* (n = 3). **j** ChIP-qPCR showing that knockout of *Chd7* increases the occupancy of PPAR-γ in the promoter regions of *Adipoq* (n = 3). Data are shown as the mean ± S.D.; p value by two-tailed Student's t test.

marrow suggested that there might be specific influences of CHD7 on adipocytes. Conditional knockout of *Chd7* in adipose tissue in vivo would be a prospective research direction. Moreover, the lack of specimens from patients was a limitation of this research. As previously reported, CHARGE syndrome is mainly caused by the *CHD7* mutation in neural crest stem cells, while patients with *CHD7* mutations in MSCs have not been studied.

In conclusion, we demonstrate that conditional knockout of *Chd7* in bone marrow MSCs leads to the activation of the PPAR signaling pathway. Such alteration would promote the MSC differentiation balance toward adipogenesis, resulting in whole body developmental disorders of the skeletal system, low bone mass, and high marrow adipose tissue. Our research provided evidence that CHD7 regulates stem cell differentiation and cell fate decisions and revealed the functional association between histone modification and osteoporosis, which might shed light on therapeutic strategies for bone pathological disorders.

Methods

Generation of conditional *Chd7* knockout mice. Based on the CRISPR-Cas9 approach, *Chd7^{fl/fl}* mice were generated with a C57BL6/J background^{55–57}. Briefly, two sgRNAs were designed to target regions either upstream or downstream of exon 2 of *Chd7* with the aid of a CRISPR design tool (<http://crispr.mit.edu>). Then, these molecules were screened for on-target activity via a Universal CRISPR Activity Assay (UCATM, Biocytogen, Inc., Beijing). Donor vectors containing LoxP flanking exon 2 mixed with sgRNAs and Cas9 mRNA were coinjected into the cytoplasm of single-celled C57BL6/J zygotes. Such injected zygotes were transferred into ovarian ducts of Kunming pseudopregnant female mice to generate F0 mice. F0 mice with the expected genotype identified by tail genomic DNA PCR and sequencing were then mated with C57BL6/J mice to obtain germline-transmitted F1 founders. Both PCR genotyping and Southern blot examination were applied to further confirm the correct genotype of the generated *Chd7^{fl/fl}* mice.

Prx1-cre and *Sp7-cre* mice were purchased from the Jackson Laboratory (Bar Harbor, ME) and were crossed with *Chd7^{fl/fl}* mice for more than three generations to obtain *Prx1-cre;Chd7^{fl/fl}* and *Sp7-cre;Chd7^{fl/fl}* conditional knockout mice^{27,28}. The genotypes were identified by PCR amplification of tail genomic DNA. Primers for the *Chd7* knockout allele and Cre transgene genotyping are listed in Supplementary Table 1. All mice were propagated and raised in specific pathogen-free facilities.

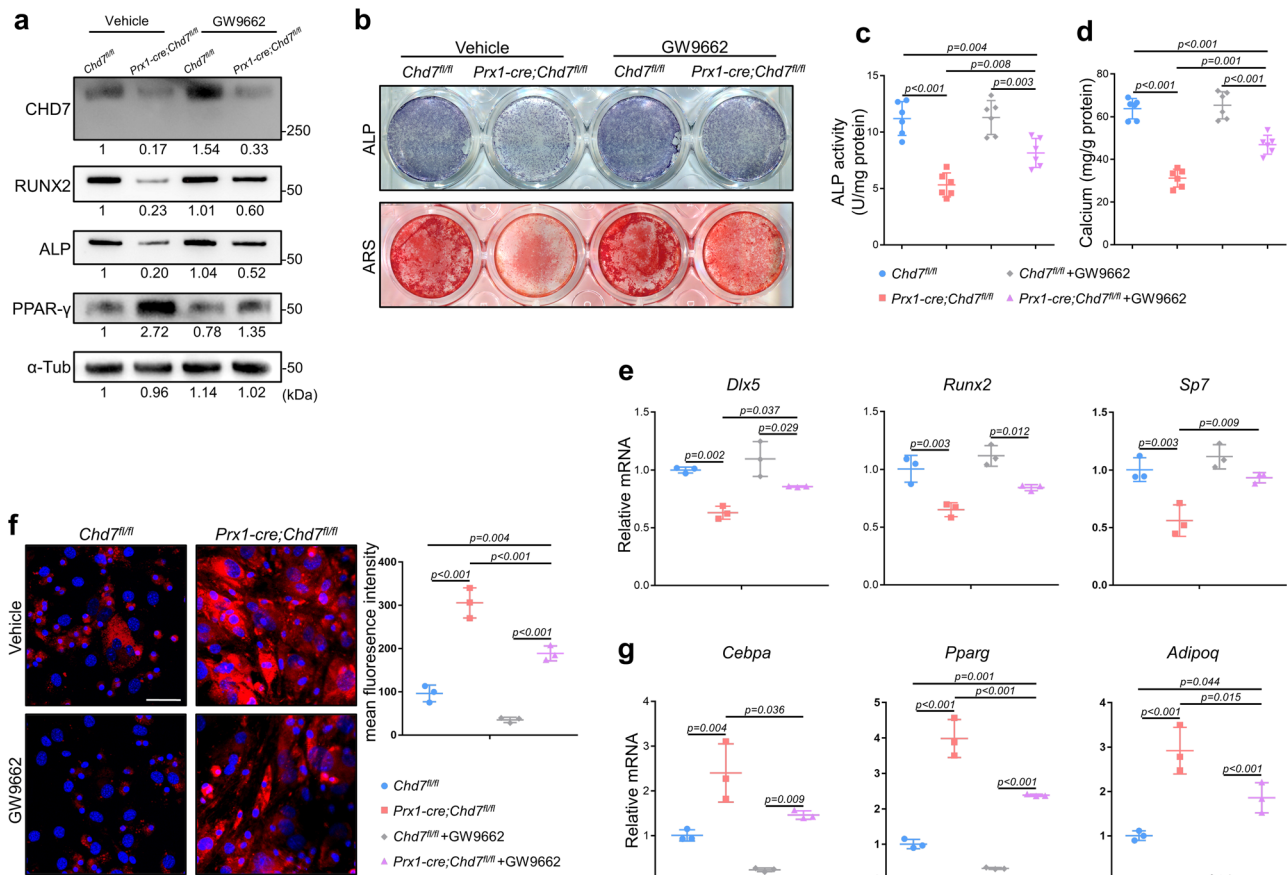


Fig. 6 PPAR- γ inhibition partially rescues the phenotype of *Chd7*-deficient MSCs. **a** Western blot analysis and quantification of CHD7, RUNX2, alkaline phosphatase, and PPAR- γ in wild type and *Chd7*-deficient bone marrow MSCs treated with vehicle or a PPAR- γ inhibitor (GW9662). **b** Representative images of ALP and ARS staining of treated MSCs. **c** Quantitative analyses of the ALP activity in treated MSCs ($n = 6$ biologically independent MSC samples). **d** Quantitative analyses of the mineralization in treated MSCs ($n = 6$ biologically independent MSC samples). **e** qRT-PCR analyses of the mRNA expression of *Dlx5*, *Runx2*, and *Sp7* in treated MSCs under osteogenic conditions ($n = 3$ biologically independent MSC samples). **f** Representative images and quantitative analyses of Nile red staining in treated MSCs. Scale bar, 50 μm ($n = 3$ biologically independent MSC slides). **g** qRT-PCR analyses of the mRNA expression of *Cebpa*, *Pparg*, and *Adipoq* in treated MSCs under adipogenic conditions ($n = 3$ biologically independent MSC samples). Data are shown as the mean \pm S.D.; p value by one-way ANOVA with Tukey's post hoc tests for multiple comparisons.

Animal experiments in this study were approved by the Institutional Review Board of West China Hospital of Stomatology, Sichuan University. All studies were approved by the Subcommittee on Research and Animal Care (SRAC) of Sichuan University. All procedures were in accordance with relevant guidelines and regulations.

Whole-mount skeletal staining. Mouse pups were harvested at postnatal day 2. After removal of the skin and viscera, the whole mount of the pups was fixed with 95% ethanol. After being processed with acetone, the specimens were stained with Alcian blue (Solarbio) solution and decolorized with 70% and 95% ethanol. After being processed with potassium hydroxide solution, the specimens were stained with Alizarin Red S (ARS) (Solarbio) solution. After being processed with potassium hydroxide solution and glycerol, the specimens were imaged with an Epson Perfection V370 Photo Scanner. Length of humeri, femurs, and tibiae was measured with ImageJ (National Institutes of Health)⁵⁸.

MicroCT. Mice were sacrificed at 4 weeks old and intraperitoneally injected with calcein (10 mg/kg of body weight; Sigma) at 7 days and 2 days before sacrifice. The collected bone tissues were fixed in 4% paraformaldehyde for 24 h and then transferred to phosphate-buffered saline (PBS) at 4 $^{\circ}\text{C}$ before scanning. According to the guidelines, microCT analysis was performed via a $\mu\text{CT}50$ microCT system (Scanco Medical, Bassersdorf, Switzerland) with a spatial resolution of 8 μm (55 kV, 114 mA, 500 ms integration time). The volume of interest (VOI) of femurs was defined as a cylindrical area at the distal region of the growth plate, 1200 μm thickness for spongiosa and 200 μm thickness for cortical bone. Bone volume was calculated within the delimited VOI. Data analysis and reconstructed images were processed on IMARIS software (version 9.1.2; Oxford Instruments). Quantification of cranial defect was calculated with ImageJ (National Institutes of Health), by

measuring the hole area in the cranium in the reconstructed images of skulls^{3,44,59,60}.

Undecalcified histomorphological analysis. After microCT scanning, femurs were successively dehydrated in 15% and 30% sucrose solutions and then embedded in NEG-50 (Thermo Scientific) at -80°C . Specimens were cut into 5- μm -thick sections with a freezing microtome (CM3050 S; Leica) with a tungsten steel blade at -35°C and were stuck to adhesive film (Cryofilm; Section-Lab Co., Ltd.).

Sections of undecalcified bone specimens were mainly processed for Von Kossa staining and analysis of double labeling. The VOI was defined as the distal end of femurs. Calcium deposits were visualized according to the Von Kossa/nuclear fast red staining method and were photographed by microscopy (BX53; Olympus). The dynamic osteogenic index was defined as the distance between 2 calcein bands by microscopy with fluorescence excitation (BX53; Olympus) and was analyzed with OsteoMeasure software (OsteoMetrics; Decatur, GA)^{26,59,61}.

Decalcified histomorphological analysis. After being fixed in 4% poly-oxymethylene for 24 h and then decalcified in 10% EDTA for 2 weeks at 4 $^{\circ}\text{C}$, femurs and tibiae were dehydrated in ethanol and xylene by Excelsior AS (Thermo Scientific). Embedded in paraffin, bone specimens were cut into 5- μm -thick sections with a paraffin microtome (RM2255; Leica)^{3,5}.

Sections of decalcified bone specimens were mainly processed for hematoxylin and eosin (HE) staining, tartrate-resistant acid phosphatase (TRAP) staining, IHC staining, and IF staining. The VOI was defined as the distal end of femurs. According to the IHC and IF staining protocol, slides were incubated in sodium citrate antigen retrieval solution at 100 $^{\circ}\text{C}$ for 10 min and then incubated with rabbit anti-CHD7 antibody (Abcam, ab117522, 1:200). IF staining slides were imaged by laser scanning confocal microscopy (FV3000; Olympus), and other

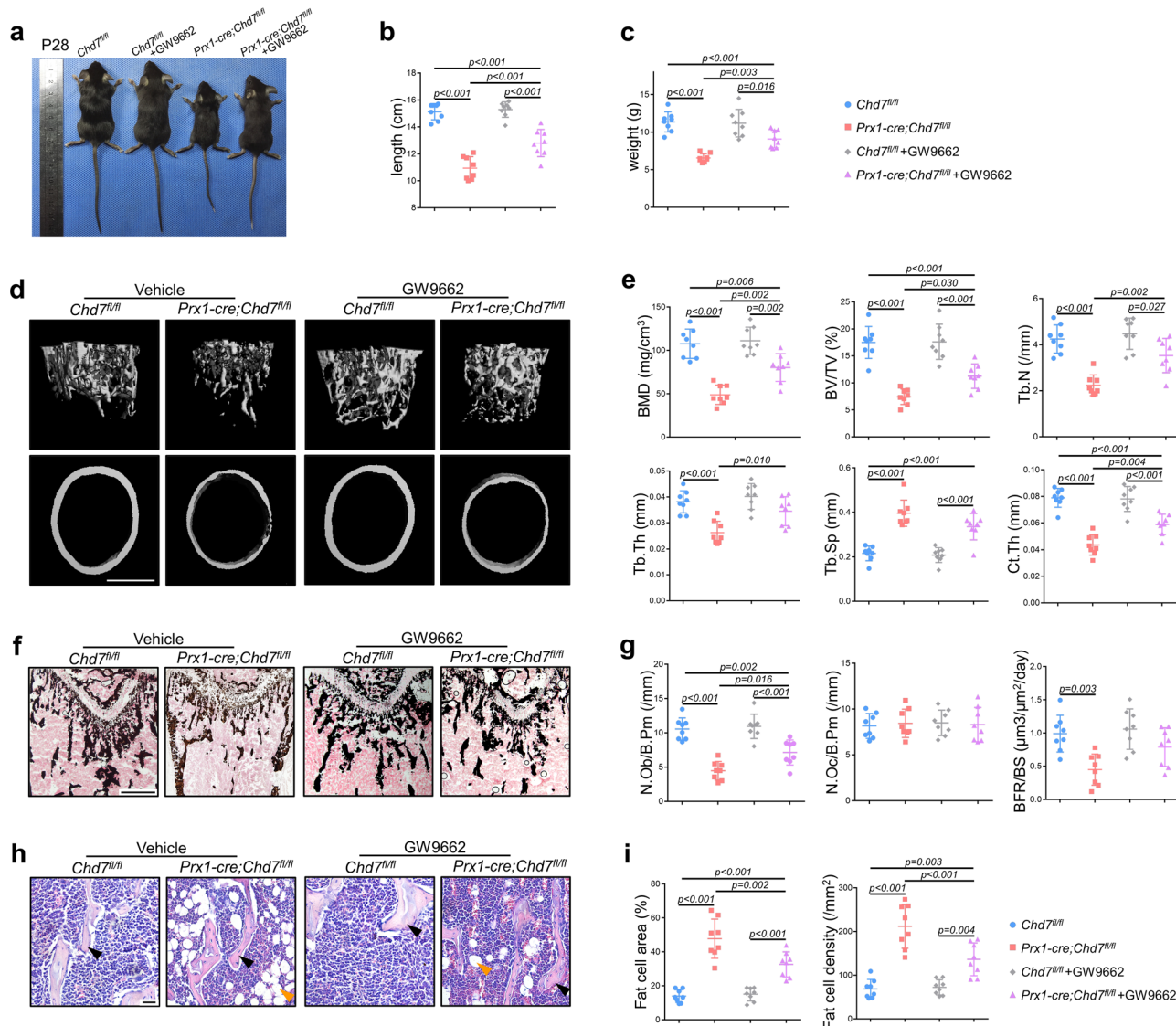


Fig. 7 Administration of a PPAR- γ inhibitor partially rescues the skeletal phenotype of *Prx1-cre;Chd7^{fl/fl}* mice. **a** Representative images of the *Chd7^{fl/fl}* and *Prx1-cre;Chd7^{fl/fl}* mice at 4 weeks old, treated with vehicle or a PPAR- γ inhibitor (GW9662) ($n = 8$). **b** Length of the treated *Chd7^{fl/fl}* and *Prx1-cre;Chd7^{fl/fl}* mice at 4 weeks old ($n = 8$). **c** Weight of the treated *Chd7^{fl/fl}* and *Prx1-cre;Chd7^{fl/fl}* mice at 4 weeks old ($n = 8$). **d** Representative microCT images of distal femurs and midshaft cortical bone from the treated *Chd7^{fl/fl}* and *Prx1-cre;Chd7^{fl/fl}* mice at 4 weeks old (Scale bar, 500 μ m). **e** Quantitative microCT analyses of the distal end of the femurs from the treated *Chd7^{fl/fl}* and *Prx1-cre;Chd7^{fl/fl}* mice at 4 weeks old ($n = 8$). **f** Von Kossa staining of trabecular bone from the femoral metaphysis in the treated *Chd7^{fl/fl}* and *Prx1-cre;Chd7^{fl/fl}* mice at 4 weeks old (Scale bar, 500 μ m). **g** Histomorphological analysis and dynamic osteogenic index of trabecular bone from the femoral metaphysis in the treated *Chd7^{fl/fl}* and *Prx1-cre;Chd7^{fl/fl}* mice at 4 weeks old, including BFR, osteoblast, and osteoclast numbers ($n = 8$). **h** Representative images and quantitative measurements of adipocytes in the distal femur marrow in the treated *Chd7^{fl/fl}* and *Prx1-cre;Chd7^{fl/fl}* mice at 4 weeks old. Black arrows indicate trabecular bones, and orange arrows indicate marrow adipose tissues (Scale bar, 50 μ m). **i** Quantitative data were obtained using the ImageJ software, including the number and area of adipocytes in the distal marrow per tissue area ($n = 8$). Data are shown as the mean \pm S.D.; p value by one-way ANOVA with Tukey's post hoc tests for multiple comparisons.

staining slides were photographed by microscopy (BX53; Olympus) and analyzed with OsteoMeasure software (OsteoMetrics; Decatur, GA)^{5,26}.

Cell culture and flow cytometry. Primary MSCs were isolated by flushing the bone marrow of femurs, tibiae, and humeri. The bone marrow suspension was cultured in 21 cm² petri dishes in alpha minimum Eagle's medium (α -MEM, HyClone) with 10% fetal bovine serum (FBS, Gibco), 100 units/mL penicillin, and 100 μ g/mL streptomycin. After incubation at 37 $^{\circ}$ C with 5% CO₂, the culture medium was changed every 48 h. MSCs at passage 3 were used for subsequent research^{3,62,63}.

After trypsin digestion, centrifugation and resuspension, the cultured cells were equally divided into five tubes. One tube was used as blank control, and the other four tubes were added with corresponding antibodies and incubated in the dark at 37 $^{\circ}$ C for 10 min. PBS were added in each tube, and then samples were loaded into

the Attune NxT Flow Cytometer (Thermo Scientific). Results were analyzed with Attune NxT Software (Thermo Scientific). The antibodies and concentrations were as follows: FITC anti-mouse/rat CD29 Antibody (BioLegend, 102205, 1:500), PE anti-mouse CD90.2 Antibody (BioLegend, 105307, 1:500), PE anti-mouse CD31 Antibody (BioLegend, 102507, 1:500), APC anti-mouse CD45 Antibody (BioLegend, 103111, 1:500).

For osteogenic induction, MSCs were cultured with osteogenic medium supplemented with 50 μ M ascorbic acid (Sigma), 10 nM dexamethasone (Sigma), and 10 mM β -glycerophosphate (Sigma). For adipogenic induction, MSCs were treated with adipogenic medium containing 10 μ g/ml insulin (Sigma), 1 μ M dexamethasone (Sigma), and 0.5 μ M isobutylmethylxanthin (Sigma)^{3,26,63}.

ALP, ARS, and Nile red staining. MSCs fixed with 4% paraformaldehyde in 24-pore plates were then stained with a BCIP/NBT Alkaline Phosphatase Color

Development Kit (Beyotime) after 7 days of osteogenic induction. The reaction was terminated after 15 min of light-free incubation at room temperature, and the pore plates were imaged with an Epson Perfection V370 Photo Scanner. Quantitative analysis of ALP activity was processed with a BCA Protein Assay Kit (Beyotime) and Alkaline Phosphatase Assay Kit (Beyotime). The BCA curve was obtained from the absorbance of the BCA protein concentration gradient. The corresponding ALP activity was calculated from the standard curve of ALP absorbance by reaction with 0.5 mM p-nitrophenyl phosphate^{59,62}.

MSCs in 24-pore plates were fixed with 4% paraformaldehyde and then stained with Alizarin Red S solution (Cayagen) at room temperature after 21 days of osteogenic induction. The pore plates were imaged with an Epson Perfection V370 Photo Scanner. The calcium nodules were detected by cetylpyridinium chloride for 15 minutes to quantify the calcium concentration. The absorbance at 562 nm was measured with a Multiskan Sky Microplate Spectrophotometer (Thermo Scientific), in contrast with the standard calcium absorbance curve^{5,26}.

For Nile red staining, MSCs on glass coverslips were fixed with 4% paraformaldehyde and then stained with Nile red solution (Solarbio) at 37 °C for 10 min after 21 days of adipogenic induction. After DAPI staining and mounting, images were obtained with laser scanning confocal microscopy (FV3000; Olympus) and were analyzed with ImageJ (National Institutes of Health)⁶⁴.

Cell immunofluorescence staining. MSCs on glass coverslips were fixed with 4% paraformaldehyde and then permeabilized with 0.5% Triton X-100 in PBS at room temperature for 10 minutes. MSCs were incubated with 1% BSA, 5% goat serum, and 0.1% Triton X-100 in PBS at room temperature for a 30-minute block. MSCs were incubated with primary antibodies from different species in blocking buffer at 4 °C overnight. After removal of the primary antibodies and rinsing with PBS the next day, MSCs were successively incubated with Alexa Fluor 488 goat anti-mouse antibody (Abcam, ab150113, 1:100) and Alexa Fluor 647 goat anti-rabbit antibody (Abcam, ab150083, 1:100) in the dark at room temperature for 1 h. After DAPI staining and mounting, images were obtained with laser scanning confocal microscopy (FV3000; Olympus) and were analyzed with ImageJ (National Institutes of Health)⁵. The primary antibodies and concentrations are as follows: mouse anti-PPAR- γ antibody (Santa Cruz, sc-271392, 1:100) and rabbit anti-trimethylhistone H3 (Lys4) antibody (CST, #9751, 1:100).

Quantitative RT-PCR and RNA-seq. Total RNA was isolated with TRIzol Reagent (Invitrogen) 5 days after osteogenic or adipogenic induction. RNA was reverse transcribed via a PrimeScript RT reagent Kit (TaKaRa). Quantitative RT-PCR was processed with SYBR Premix Ex Taq (TaKaRa) and LightCycler 96 (Roche). The housekeeping gene *GAPDH* was used as the baseline to quantitatively analyze the gene expression of the osteogenic group, and *36B4* was used for the adipogenic group^{59,62}.

For RNA sequencing, 12 RNA samples of MSCs in 4 groups were prepared according to the manufacturer's protocol of a NEBNext Ultra RNA Library Prep Kit for Illumina (USA). RNA samples were subjected to HiSeq 2500 (Illumina). FastQC (v0.11.5) and the FASTX toolkit (0.0.13) were applied for quality control. Further analysis, e.g., KEGG enrichment, GO enrichment, heatmaps, and GSEA, was performed to explore the downstream pathways on this basis^{3,26}.

Western blot and co-IP. The total protein of MSCs was collected with a protein extraction kit (PE001, SAB Biotech) and was then heated with SDS-PAGE Sample Loading Buffer (Beyotime) at 100 °C for 5 min. After gel electrophoresis separation, protein was transferred to a PVDF membrane (Millipore) via Bio-Rad Powerpac HC. After antigen blocking, the membranes were incubated with the primary antibody described below at 4 °C overnight. After a 1-h incubation with HRP-labeled goat anti-rabbit IgG or goat anti-mouse IgG (Beyotime) at room temperature, the membranes were exposed via ChemiDoc XRS+ (Bio-Rad) to detect the designated protein expression level. The primary antibodies and concentrations were as follows: rabbit anti- α -tubulin antibody (Beyotime, AF0001, 1:5000), rabbit anti-CHD7 antibody (Abcam, ab117522, 1:1000), mouse anti-RUNX2 antibody (Santa Cruz, sc-101145, 1:1000), mouse anti-alkaline phosphatase antibody (Santa Cruz, sc-271431, 1:1000), rabbit anti-PPAR- γ antibody (CST, #2443, 1:1000), mouse anti-PPAR- γ antibody (Santa Cruz, sc-271392, 1:1000), and rabbit anti-trimethylhistone H3 (Lys4) antibody (CST, #9751, 1:1000)^{3,62}.

For the co-IP assay, MSCs were lysed in mild lysis buffer (MLB) with protease/phosphatase inhibitor cocktail (CST, #5872, 1:100) for 10 min with gentle shaking at 4 °C. After centrifugation at 14,000 $\times g$ for 10 min, 10% of the supernatant was heated with SDS-PAGE sample loading buffer (Beyotime) at 100 °C for 5 min as input. The remaining 90% of supernatant was collected and incubated with IgG or selected antibody overnight at 4 °C with mixing. After washes with MLB, 5 μ g Pierce Protein A/G Magnetic Beads (Thermo Scientific) was added to each sample and incubated for 1 h at 4 °C with mixing. After collection and washing, the beads were heated with SDS-PAGE Sample Loading Buffer (Beyotime) at 100 °C for 5 min for subsequent western blot analysis. The co-IP antibodies were rabbit (DAIE) mAb IgG XP® Isotype Control (CST, #3900, 1:100) and rabbit anti-PPAR- γ antibody (CST, #2443, 1:100)⁶⁵.

ChIP assay. ChIP-seq data were obtained from GSM2104246 and GSM1571714 and were analyzed with WashU EpiGenome Browser (Washington University) to ascertain the binding site and the experimental design of ChIP-PCR^{29,30}. According to the manufacturer's protocol of the Magna ChIP HiSens Chromatin Immunoprecipitation kit (Millipore), 2×10^6 cells were harvested in each ChIP reaction. Protein and DNA of each sample were crosslinked by applying 37% formaldehyde solution. SDS lysis buffer with protease/phosphatase inhibitor cocktail (CST, 1:100) was added after cell harvesting. After restriction enzyme digestion, centrifugation, and precipitation with beads, the precipitated DNA samples were quantified with specific primers via real-time PCR⁵.

Rescue strategy in vitro and in vivo. Based on the verification of PPAR- γ signaling pathway, MSCs were treated with a PPAR- γ specific antagonist GW9662 (MedChemExpress) to rescue the phenotype in vitro. The application concentration was 10 μ M, dissolved in DMSO⁶⁶.

To partially rescue the general body phenotype in vivo, we intraperitoneally injected 3 mg/kg/day GW9662 into the female *Prx1-cre;Chd7^{fl/fl}* and control littermates from postnatal day 10 until 4 weeks old before sacrifice. Hereafter, microCT and decalcified histomorphological analyses were conducted on the specimens to clarify the rescue effect^{67,68}.

Statistical analyses. All data were calculated as the mean \pm standard deviation (SD). Statistical differences were analyzed via Student's *t* test for independent sample tests or one-way ANOVA with Tukey's post hoc tests for multiple comparisons. A *p* value <0.05 was considered statistically significant^{3,62}.

Reporting summary. Further information on research design is available in the Nature Research Reporting Summary linked to this article.

Data availability

The data that support this study are available from the corresponding authors upon reasonable request. The RNA-seq data generated in this study have been deposited in the NCBI database under accession code [GSE167886](https://doi.org/10.1038/s41467-022-29633-6). The ChIP-seq data were obtained from the publicly available sequencing datasets in NCBI database under accession code [GSM2104246](https://doi.org/10.1038/s41467-022-29633-6) and [GSM1571714](https://doi.org/10.1038/s41467-022-29633-6). Source data are provided with this paper.

Received: 21 April 2021; Accepted: 23 March 2022;

Published online: 13 April 2022

References

- Salhotra, A., Shah, H., Levi, B. & Longaker, M. Mechanisms of bone development and repair. *Nat. Rev. Mol. Cell Biol.* **21**, 696–711 (2020).
- Guan, M. et al. Directing mesenchymal stem cells to bone to augment bone formation and increase bone mass. *Nat. Med.* **18**, 456–462 (2012).
- Wu, Y. et al. Mettl3-mediated mA RNA methylation regulates the fate of bone marrow mesenchymal stem cells and osteoporosis. *Nat. Commun.* **9**, 4772 (2018).
- Ensrud, K. E. Bisphosphonates for postmenopausal osteoporosis. *JAMA* **325**, 96–96 (2021).
- Wang, Y. et al. Alpha-ketoglutarate ameliorates age-related osteoporosis via regulating histone methylations. *Nat. Commun.* **11**, 5596 (2020).
- van Gestel, N. et al. Lipid availability determines fate of skeletal progenitor cells via SOX9. *Nature* **579**, 111–117 (2020).
- Rother, M. et al. CHD7 and 53BP1 regulate distinct pathways for the re-ligation of DNA double-strand breaks. *Nat. Commun.* **11**, 5775 (2020).
- Gervais, L. et al. Stem cell proliferation is kept in check by the chromatin regulators Kismet/CHD7/CHD8 and Trr/MLL3/4. *Developmental cell* **49**, 556–573.e556 (2019).
- Whittaker, D. et al. The chromatin remodeling factor CHD7 controls cerebellar development by regulating reelin expression. *J. Clin. Investig.* **127**, 874–887 (2017).
- Feng, W. et al. Chd7 is indispensable for mammalian brain development through activation of a neuronal differentiation programme. *Nat. Commun.* **8**, 14758 (2017).
- He, D. et al. Chd7 cooperates with Sox10 and regulates the onset of CNS myelination and remyelination. *Nat. Neurosci.* **19**, 678–689 (2016).
- Ghaoui, R. et al. Use of whole-exome sequencing for diagnosis of limb-girdle muscular dystrophy: outcomes and lessons learned. *JAMA Neurol.* **72**, 1424–1432 (2015).
- Butcher, D. et al. CHARGE and Kabuki syndromes: gene-specific DNA methylation signatures identify epigenetic mechanisms linking these clinically overlapping conditions. *Am. J. Hum. Genet.* **100**, 773–788 (2017).

14. Basson, M. & van Ravenswaaij-Arts, C. Functional insights into chromatin remodelling from studies on CHARGE syndrome. *Trends Genet.: TIG* **31**, 600–611 (2015).
15. Van Nostrand, J. et al. Inappropriate p53 activation during development induces features of CHARGE syndrome. *Nature* **514**, 228–232 (2014).
16. Pagon, R., Graham, J., Zonana, J. & Yong, S. Coloboma, congenital heart disease, and choanal atresia with multiple anomalies: CHARGE association. *J. Pediatrics* **99**, 223–227 (1981).
17. Bajpai, R. et al. CHD7 cooperates with PBAF to control multipotent neural crest formation. *Nature* **463**, 958–962 (2010).
18. Gao, X. et al. CHD7 gene polymorphisms are associated with susceptibility to idiopathic scoliosis. *Am. J. Hum. Genet.* **80**, 957–965 (2007).
19. Tahara, T. et al. Colorectal carcinomas with CpG island methylator phenotype 1 frequently contain mutations in chromatin regulators. *Gastroenterology* **146**, 530–538.e535 (2014).
20. Schnetz, M. et al. Genomic distribution of CHD7 on chromatin tracks H3K4 methylation patterns. *Genome Res.* **19**, 590–601 (2009).
21. Chen, Y., Wang, M., Chen, D., Wang, J. & Kang, N. Chromatin remodeling enzyme CHD7 is necessary for osteogenesis of human mesenchymal stem cells. *Biochem. Biophys. Res. Commun.* **478**, 1588–1593 (2016).
22. Eleftheriou, F. & Yang, X. Genetic mouse models for. *Bone Stud.–Strengths Limit. Bone* **49**, 1242–1254 (2011).
23. Fan, Y. et al. Parathyroid hormone directs bone marrow mesenchymal cell fate. *Cell Metab.* **25**, 661–672 (2017).
24. Yue, R., Zhou, B., Shimada, I., Zhao, Z. & Morrison, S. Leptin receptor promotes adipogenesis and reduces osteogenesis by regulating mesenchymal stromal cells in adult bone marrow. *cell stem cell* **18**, 782–796 (2016).
25. Isaac, J. et al. DLX3 regulates bone mass by targeting genes supporting osteoblast differentiation and mineral homeostasis in vivo. *Cell Death Differ.* **21**, 1365–1376 (2014).
26. Guo, Y. et al. Ubiquitin-specific protease USP34 controls osteogenic differentiation and bone formation by regulating BMP2 signaling. *EMBO J.* **37**, <https://doi.org/10.15252/embj.201899398> (2018).
27. Logan, M. et al. Expression of Cre Recombinase in the developing mouse limb bud driven by a Prxl enhancer. *Genes* **33**, 77–80 (2002).
28. Rodda, S. & McMahon, A. Distinct roles for Hedgehog and canonical Wnt signaling in specification, differentiation and maintenance of osteoblast progenitors. *Development* **133**, 3231–3244 (2006).
29. Meyer, M., Benkuský, N., Sen, B., Rubin, J. & Pike, J. Epigenetic plasticity drives adipogenic and osteogenic differentiation of marrow-derived mesenchymal stem cells. *J. Biol. Chem.* **291**, 17829–17847 (2016).
30. Soccio, R. et al. Genetic variation determines PPAR γ function and anti-diabetic drug response in vivo. *Cell* **162**, 33–44 (2015).
31. Chandra, V. et al. Promoter-interacting expression quantitative trait loci are enriched for functional genetic variants. *Nat. Genet.* **53**, 110–119 (2021).
32. Torres-Garcia, S. et al. Epigenetic gene silencing by heterochromatin primes fungal resistance. *Nature* **585**, 453–458 (2020).
33. Cebianca, D. et al. Active chromatin marks drive spatial sequestration of heterochromatin in *C. elegans* nuclei. *Nature* **569**, 734–739 (2019).
34. Ai, S. et al. Profiling chromatin states using single-cell HiChIP-seq. *Nat. Cell Biol.* **21**, 1164–1172 (2019).
35. Inoue, F., Kreimer, A., Ashuach, T., Ahituv, N. & Yosef, N. Identification and massively parallel characterization of regulatory elements driving neural induction. *cell stem cell* **25**, 713–727.e710 (2019).
36. Raganathan, K., Jih, G. & Moazed, D. Epigenetic inheritance uncoupled from sequence-specific recruitment. *Science* **348**, 1258699 (2015).
37. Latham, J., Chosed, R., Wang, S. & Dent, S. Chromatin signaling to kinetochores: transregulation of Dam1 methylation by histone H2B ubiquitination. *Cell* **146**, 709–719 (2011).
38. Wang, G. et al. Haematopoietic malignancies caused by dysregulation of a chromatin-binding PHD finger. *Nature* **459**, 847–851 (2009).
39. Flanagan, J. et al. Double chromodomains cooperate to recognize the methylated histone H3 tail. *Nature* **438**, 1181–1185 (2005).
40. Yu, R., Wang, X. & Moazed, D. Epigenetic inheritance mediated by coupling of RNAi and histone H3K9 methylation. *Nature* **558**, 615–619 (2018).
41. Wang, X. & Moazed, D. DNA sequence-dependent epigenetic inheritance of gene silencing and histone H3K9 methylation. *Science* **356**, 88–91 (2017).
42. Jih, G. et al. Unique roles for histone H3K9me states in RNAi and heritable silencing of transcription. *Nature* **547**, 463–467 (2017).
43. Ye, L. et al. Histone demethylases KDM4B and KDM6B promotes osteogenic differentiation of human MSCs. *Cell Stem Cell* **11**, 50–61 (2012).
44. Deng, P. et al. Loss of KDM4B exacerbates bone-fat imbalance and mesenchymal stromal cell exhaustion in skeletal aging. *Cell Stem Cell* **28**, 1057–1073.e1057 (2021).
45. Augert, A. et al. Small cell lung cancer exhibits frequent inactivating mutations in the histone methyltransferase KMT2D/MLL2: CALGB 151111 (alliance). *J. Thorac. Oncol.* **12**, 704–713 (2017).
46. Mondal, T. et al. Sense-antisense lncRNA pair encoded by locus 6p22.3 determines neuroblastoma susceptibility via the USP36-CHD7-SOX9 regulatory axis. *Cancer Cell* **33**, 417–434.e417 (2018).
47. Liu, C., Kang, N., Guo, Y. & Gong, P. Advances in chromodomain helicase DNA-binding (CHD) proteins regulating stem cell differentiation and human diseases. *Front. Cell Develop. Biol.* **9**, 710203 (2021).
48. Kim, H. et al. Mutations in CHD7, encoding a chromatin-remodeling protein, cause idiopathic hypogonadotropic hypogonadism and Kallmann syndrome. *Am. J. Hum. Genet.* **83**, 511–519 (2008).
49. Pleasance, E. et al. A small-cell lung cancer genome with complex signatures of tobacco exposure. *Nature* **463**, 184–190 (2010).
50. Visser, L. et al. Mutations in a new member of the chromodomain gene family cause CHARGE syndrome. *Nat. Genet.* **36**, 955–957 (2004).
51. Jambhekar, A., Dhall, A. & Shi, Y. Roles and regulation of histone methylation in animal development. *Nat. Rev. Mol. Cell Biol.* **20**, 625–641 (2019).
52. Cortese, R. et al. DNA methylation profiling of blood monocytes in patients with obesity hypoventilation syndrome: effect of positive airway pressure treatment. *Chest* **150**, 91–101 (2016).
53. Takada, I., Yogiashi, Y. & Kato, S. Signaling crosstalk between PPAR γ and BMP2 in mesenchymal stem cells. *PPAR Res.* **2012**, 607141 (2012).
54. Hong, J. et al. TAZ, a transcriptional modulator of mesenchymal stem cell differentiation. *Science* **309**, 1074–1078 (2005).
55. Kim, D. et al. Digenome-seq: genome-wide profiling of CRISPR-Cas9 off-target effects in human cells. *Nat. Methods* **12**, 237–243 (2015).
56. Cong, L. et al. Multiplex genome engineering using CRISPR/Cas systems. *Science* **339**, 819–823 (2013).
57. Mali, P. et al. RNA-guided human genome engineering via Cas9. *Science* **339**, 823–826 (2013).
58. Rigueur, D. & Lyons, K. Whole-mount skeletal staining. *Methods Mol. Biol.* **1130**, 113–121 (2014).
59. Sheng, R. et al. METTL3-mediated m⁶A mRNA methylation modulates tooth root formation by affecting NFIC translation. *J. Bone Mineral Res.* <https://doi.org/10.1002/jbmr.4180> (2020).
60. Bouxsein, M. et al. Guidelines for assessment of bone microstructure in rodents using micro-computed tomography. *J. Bone Miner. Res.* **25**, 1468–1486 (2010).
61. Zhang, D. et al. LepR-expressing stem cells are essential for alveolar bone regeneration. *J. Dent. Res.* **99**, 1279–1286 (2020).
62. Li, Q. et al. Ubiquitin-specific protease 34 inhibits osteoclast differentiation by regulating NF- κ B signaling. *J. Bone Miner. Res.* **35**, 1597–1608 (2020).
63. Liu, C., Li, Q., Xiao, Q., Gong, P. & Kang, N. CHD7 regulates osteogenic differentiation of human dental follicle cells via PTH1R signaling. *Stem Cells Int.* **2020**, 8882857 (2020).
64. Zhang, Z. et al. Upregulation of miR-125b by estrogen protects against non-alcoholic fatty liver in female mice. *J. Hepatol.* **63**, 1466–1475 (2015).
65. Besse, A. et al. The GABA transaminase, ABAT, is essential for mitochondrial nucleoside metabolism. *Cell Metab.* **21**, 417–427 (2015).
66. Byndloss, M. et al. Microbiota-activated PPAR- γ signaling inhibits dysbiotic Enterobacteriaceae expansion. *Science* **357**, 570–575 (2017).
67. Tobiasova, Z. et al. Peroxisome proliferator-activated receptor- γ agonists prevent in vivo remodeling of human artery induced by alloreactive T cells. *Circulation* **124**, 196–205 (2011).
68. Diano, S. et al. Peroxisome proliferation-associated control of reactive oxygen species sets melanocortin tone and feeding in diet-induced obesity. *Nat. Med.* **17**, 1121–1127 (2011).

Acknowledgements

We thank Dr. Quan Yuan from the State Key Laboratory of Oral Diseases, Sichuan University, for the valuable advice. We thank Dr. Qiang Guo from the State Key Laboratory of Oral Diseases, Sichuan University, for assistance with microCT scanning. We thank Dr. Yi Fan from the State Key Laboratory of Oral Diseases, Sichuan University, for the provision of reporter mouse samples. This research was supported by the National Natural Science Foundation of China (NSFC grant numbers 81701009 and 82170935).

Author contributions

L.C. conceived, designed, performed and analyzed the experiments, and drafted the work; X.Q. and L.Q. designed the experiments and revised the draft; L.W. analyzed the data; J.S., Z.D., W.Y., and D.X. participated in in vitro experiments and data interpretation; G.P. and K.N. conceived, designed the work, secured funding, and revised the draft. All authors reviewed the manuscript.

Competing interests

The authors declare no competing interests.

Additional information

Supplementary information The online version contains supplementary material available at <https://doi.org/10.1038/s41467-022-29633-6>.

Correspondence and requests for materials should be addressed to Ping Gong or Ning Kang.

Peer review information *Nature Communications* thanks Songtao Shi and the other, anonymous, reviewer(s) for their contribution to the peer review of this work.

Reprints and permission information is available at <http://www.nature.com/reprints>

Publisher's note Springer Nature remains neutral with regard to jurisdictional claims in published maps and institutional affiliations.



Open Access This article is licensed under a Creative Commons Attribution 4.0 International License, which permits use, sharing, adaptation, distribution and reproduction in any medium or format, as long as you give appropriate credit to the original author(s) and the source, provide a link to the Creative Commons license, and indicate if changes were made. The images or other third party material in this article are included in the article's Creative Commons license, unless indicated otherwise in a credit line to the material. If material is not included in the article's Creative Commons license and your intended use is not permitted by statutory regulation or exceeds the permitted use, you will need to obtain permission directly from the copyright holder. To view a copy of this license, visit <http://creativecommons.org/licenses/by/4.0/>.

© The Author(s) 2022